Available online at www.sciencedirect.com
ScienceDirect
International Journal of Heat and Fluid Flow 28 (2007) 821–837
International Journal of HEAT AND FLUID FLOW
www.elsevier.com/locate/ijhff

Numerical study of transient laminar natural convection over an isothermal sphere

Shu Yang, Vasudevan Raghavan, George Gogos *

Department of Mechanical Engineering, N104 Walter Scott Engineering Center, University of Nebraska-Lincoln, Lincoln, NE 68588-0656, USA

Received 21 May 2006; received in revised form 29 July 2006; accepted 25 August 2006
Available online 19 October 2006

Abstract

The full Navier–Stokes equations and the energy equation for laminar natural convection heat transfer over an isothermal sphere have been discretized using the finite control volume formulation and solved by employing the SIMPLEC method. Transient and "steady-state" results have been obtained for a wide range of high Grashof numbers ($10^5 \leqslant Gr \leqslant 10^9$) and a wide range of Prandtl numbers ($Pr = 0.02$, 0.7, 7 and 100). Main results are listed below. A plume with a mushroom-shaped cap forms above the sphere and drifts upward continuously with time. The upward movement of the plume cap is slowed as the Prandtl number increases. The size and the level of temperature of the transient cap and plume stem decrease with increasing Gr and Pr. The time at which the "steady-state" is reached, increases with the Prandtl number. The presence of a vortex in the wake of the sphere has been predicted and has been clearly delineated as a function of both Grashof and Prandtl numbers. The overall Nusselt numbers and total drag coefficients for the range of Grashof and Prandtl numbers investigated are presented and they are in very good agreement with studies available in the literature.

Keywords: Natural convection; Laminar; Isothermal sphere; Numerical solutions; Vortex; Drag

1. Introduction

Natural convection over a sphere is relevant in many practical applications such as combustion and vaporization of fuel droplets, spray drying, packed beds of spherical bodies etc. There are fundamental unanswered questions concerning the nature of flow separation due to natural convection from spheres. The curvature effect inherent to a sphere surface contributes to rapid growth of the boundary layer followed by a flow separation as the momentum of the fluid becomes sufficiently high to overcome the increase in pressure. Consequently, the boundary layer assumptions are invalid in such a region. The full Navier–Stokes equations need to be employed to investigate the plume development and the recirculation vortex that may be present in the wake of the sphere.

Although numerous analytical, computational and experimental investigations have been conducted on laminar natural convection adjacent to a vertical flat plate, only limited literature is available for natural convection over spheres. Early analytical studies on natural convection over a sphere considered limiting cases of either high Grashof number by employing boundary layer theory or very low Grashof number by employing asymptotic expansion techniques (Chiang et al., 1964; Singh and Hasan, 1983; Gebhart et al., 1988). The full Navier–Stokes equations (without the boundary layer assumptions) and energy equation of laminar natural convection over a sphere were first solved numerically by Geoola and Cornish (1981, 1982) for $0.05 \leqslant Gr \leqslant 12500$ and Pr of 0.72, 10 and 100. Farouk (1983) solved the complete steady Navier–Stokes equations to obtain local and overall heat transfer results for small and moderate Rayleigh numbers ($10^{-1} \leqslant Ra_D \leqslant 10^4$). Fujii et al. (1984) presented transient results for $Ra_D = 100$ and $Pr = 0.72$. Riley (1986) provided transient solutions for $10^2 \leqslant Gr \leqslant 10^4$ and $Pr = 0.72$ and 7.0. Dudek

* Corresponding author. Tel.: +1 402 472 3006; fax: +1 402 472 1465.
E-mail address: ggogos1@unlnotes.unl.edu (G. Gogos).

0142-727X/$ - see front matter © 2006 Elsevier Inc. All rights reserved.
doi:10.1016/j.ijheatfluidflow.2006.08.004

Nomenclature

C_D	total drag coefficient
$C_{D,p}$	pressure drag coefficient
$C_{D,\mu}$	viscous drag coefficient
c'_p	specific heat capacity at constant pressure
$\vec{F}'$	body force in momentum equation
F'_D	drag force
g'	acceleration due to gravity
Gr	Grashof number
h'_θ	local heat transfer coefficient
$\bar{h}'$	average heat transfer coefficient
k'	thermal conductivity
Nu	overall Nusselt number
Nu_θ	local Nusselt number
p'_d	motion pressure
Pr	Prandtl number
r	spherical radial coordinate
R, R'_0	sphere radius
Ra	Rayleigh number
Ra_D	Rayleigh number based on diameter
r_∞, z_∞	outer computational boundary
t	time
T'	dimensional temperature
T_s	surface temperature
$\vec{V}$	velocity vector
V_r	radial velocity
V_θ	polar velocity
X, Y, Z	Cartesian coordinates
z	radial transformed coordinate

Greek symbols

β'	coefficient of thermal volumetric expansion
Γ_z, Γ_θ	diffusion coefficients in general governing differential equation
δ_{source}	source term in general governing differential equation
δ_H	hydrodynamic boundary layer thickness
δ_T	thermal boundary layer thickness
θ	spherical polar coordinate
μ'	absolute viscosity
ν'	kinematic viscosity
ξ	non-dimensional temperature
ρ'	density
σ	dependent variable in general differential equation
ψ	non-dimensional stream function
ω	non-dimensional vorticity function

Subscripts

∞	ambient condition
s	surface conditions

Superscripts

$'$	dimensional value

et al. (1988) obtained drag coefficients both numerically and experimentally for a range of small Grashof numbers ($10^{-4} \leqslant Gr \leqslant 0.5$). Jia and Gogos (1996a,b) conducted a study over a wide range of Grashof numbers ($10 \leqslant Gr \leqslant 10^8$) and predicted flow separation and an associated vortex in the wake of the sphere for large Grashof numbers. A stream function-vorticity formulation was adopted and results presented were mostly limited to $Pr = 0.72$.

With regards to experimental work, a number of investigations have been conducted. Overall Nusselt number (Nu) was presented for a wide range of Grashof numbers and/or Rayleigh numbers by Yuge (1960), Mathers et al. (1957), Amato and Tien (1972) and Kyte et al. (1953). Flow separation was observed by Kranse and Schenk (1965) for high Grashof number ($10^8 < Gr_D < 10^9$). Their study involved melting of a solid benzene sphere in benzene liquid ($Pr = 8.3$). They found that the local Nusselt number first decreases with θ, reaches a minimum and then increases near the rear stagnation. The same phenomenon was also observed by Schenk and Schenkels (1968) in their experiment of an ice sphere melting in water ($Pr = 7$). Shlien and Boxman (1980) measured the temperature field of a laminar starting plume. They reported that a starting plume with a mushroom-shaped cap rises from a heating source and the column of fluid following the cap has the same temperature distribution as the steady plume.

Jaluria and Gebhart (1975) investigated experimentally natural convection over a hemisphere in water ($10^7 \leqslant Gr_D \leqslant 3 \times 10^8$ and $Pr = 7$). Velocity and temperature profiles were determined. The centerline velocity within the plume increased rapidly close to the sphere surface. A sharp drop in centerline temperature within the plume was observed very close to the surface. The local Nusselt number, after presenting a minimum, increased rapidly as the flow approached the top of the hemisphere. No flow reversal was observed in their investigation.

From the literature survey presented above, it is clear that most of the earlier investigators have mostly considered wide range of Gr but limited their studies to a single Prandtl number (Fujii et al., 1984; Jia and Gogos, 1996a,b; Kranse and Schenk, 1965; Schenk and Schenkels, 1968; Shlien and Boxman, 1980; Jaluria and Gebhart, 1975). Also, only a few investigators have carried out transient analysis. In order to address the fundamental unanswered questions concerning the transient nature of flow due to natural convection from isothermal spheres, the

present study has been carried out. For this purpose a numerical model has been developed to solve the complete time-dependent Navier–Stokes equations along with the energy equation using the finite-volume method (Patankar, 1980) and the SIMPLEC method (Van Doormaal and Raithby, 1984). The numerical model employs the primitive variables to study the flow and temperature distributions over the sphere. A wide range of high Grashof numbers ($10^5 \leqslant Gr \leqslant 10^9$) and a wide range of Prandtl numbers ($Pr = 0.02$, 0.7, 7 and 100), have been considered in this study. The numerical simulations reveal flow separation at the top of the sphere. The presence of flow separation and an associated vortex in the wake of the sphere is clearly dictated by both Grashof and Prandtl numbers. Transient as well as "steady-state" values of the Nusselt numbers and the total drag coefficients are also presented. In this study, execution of the simulations has been terminated when "steady-state" is reached, namely, the variations in all the variables with respect to time become negligible in the computational domain under consideration.

2. Theoretical model

A sphere of fixed radius R'_0 held at a steady and uniform temperature of T_s is suddenly introduced into a cold and stagnant fluid environment maintained at temperature and pressure of T'_∞ and p'_∞. Gradually, the buoyancy effect induces an upward axisymmetric flow field around the sphere. Near the top of the sphere, hot fluid rises and forms into an evolving plume.

The simulations have been carried out using the following assumptions: (a) the sphere is kept stationary at all times, (b) the fluid is Newtonian, of infinite extent, and contains a single, inert chemical compound, (c) the flow is buoyancy-driven, laminar and axisymmetric, and (d) the bulk viscosity coefficient, radiation effects, viscous dissipation and compressibility effects are negligible. The assumption that the flow is axisymmetric may not be completely valid for high speed flows, especially for large Grashof and Prandtl numbers. However, the predictions regarding integrated surface quantities agree well with experimental results available in the literature (presented later). Regarding the transition to turbulence, it is a well known fact that for horizontal cylinders, the critical Rayleigh number ($GrPr$) is around 10^9. However, it is assumed in general, that in the range the $10^4 < GrPr < 10^{10}$ flow is laminar and in the range of $10^9 < GrPr < 10^{12}$, it is turbulent, since there is no clear cut delineation for a particular value of the Rayleigh number at which transition may occur. The flow behaves similarly for the sphere case. Thus, it should be cautioned here that for the extreme case of $Pr = 100$ and $Gr = 10^9$ considered, the laminar assumption may not be completely valid.

Throughout the present study, the notation of prime is used to indicate dimensional values. The dimensional governing equations for an incompressible fluid with constant properties can be written in vector form:

$$\nabla' \cdot \vec{V}' = 0 \tag{1}$$

$$\rho' \frac{\partial \vec{V}'}{\partial t'} + \rho'(\vec{V}' \cdot \nabla')\vec{V}' = -\nabla' p' + \vec{F}' + \mu' \nabla'^2 \vec{V}' \tag{2}$$

$$\rho' c'_p \left[\frac{\partial T'}{\partial t'} + (\vec{V}' \cdot \nabla')T' \right] = k' \nabla'^2 T' \tag{3}$$

where $\vec{V}'$ is the velocity vector, $\vec{F}'$ is the body force, ρ' is the density, t' is the time, p' is the pressure, T' is the temperature, and μ', c'_p and k' are viscosity, heat capacity at constant pressure and thermal conductivity, respectively. Employing the Boussinesq approximations, the terms $(-\nabla' p' + \vec{F}')$ can be replaced by $-g'\rho'\beta'(T' - T'_\infty) - \nabla' p'_d$, where g' is acceleration due to gravity, p'_d is the motion pressure and $\beta' = -\frac{1}{\rho'}\left(\frac{\partial \rho'}{\partial T'}\right)_{p'}$ is the coefficient of thermal volumetric expansion.

Employing spherical coordinates (r', θ), the physical geometry and the surrounding fluid flow are illustrated in Fig. 1. The above equations along with appropriate boundary conditions can be cast in dimensionless form using:

$$r = \frac{r'}{R'_0} = e^z; \quad t = \frac{V_{\text{ref}}}{R'_0} t'; \quad p_d = \frac{p'_d}{\frac{1}{2}\rho' V^2_{\text{ref}}};$$
$$V_r = \frac{V'_r}{V_{\text{ref}}}; \quad V_\theta = \frac{V'_\theta}{V_{\text{ref}}}; \quad \xi = \frac{T' - T'_\infty}{T'_s - T'_\infty}$$

where V'_r and V'_θ are the radial and polar fluid velocity components and ξ is the non-dimensional temperature. The reference velocity V_{ref} is given in terms of Grashof number ($V_{\text{ref}} = \frac{\nu'}{R'_0} Gr^{1/2}$, where $Gr = \frac{R'^3_0 g' \beta' (T'_s - T')}{\nu'^2}$), where ν' is the kinematic viscosity.

An exponential function for the non-dimensional radius ($r = e^z$) is used to produce finer grids near the surface of the

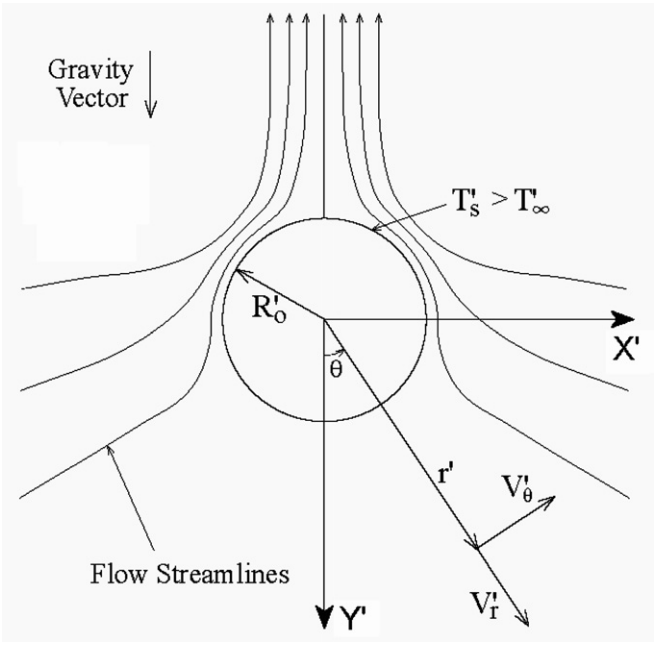

Fig. 1. Buoyancy-driven flow over a sphere.

sphere, where pressure, velocity and temperature gradients are the largest. Using the exponential function, Eqs. (1)–(3) may be rearranged and cast into a single generalized dimensionless differential equation of the form:

$$\frac{\partial}{\partial t}(\rho\sigma e^{3z}\sin\theta)+\frac{\partial}{\partial z}(\rho V_r\sigma e^{2z}\sin\theta)+\frac{\partial}{\partial\theta}(\rho V_\theta\sigma e^{2z}\sin\theta)$$
$$=\frac{\partial}{\partial z}\left(\Gamma_z e^{z}\sin\theta\frac{\partial\sigma}{\partial z}\right)+\frac{\partial}{\partial\theta}\left(\Gamma_\theta e^{z}\sin\theta\frac{\partial\sigma}{\partial\theta}\right)+\delta_{\text{source}} \quad (4)$$

where σ is the dependent variable of interest and Γ_z and Γ_θ are the radial and polar diffusion coefficients, respectively. The values of σ, Γ_z, Γ_θ and δ_{source} for the conservation equations are given below.

(a) Mass continuity equation

$$\sigma=1;\quad \Gamma_z=\Gamma_\theta=0;\quad \delta_{\text{source}}=0 \quad (5)$$

(b) Radial momentum

$$\sigma=V_r;\quad \Gamma_z=\Gamma_\theta=1/Gr^{1/2}$$
$$\delta_{\text{source}}=V_\theta^2e^{2z}\sin\theta-e^{2z}\sin\theta\frac{\partial p_d}{\partial z}-\xi e^{3z}\cos\theta\sin\theta+\frac{1}{Gr^{\frac{1}{2}}}\left[-2\frac{\partial}{\partial\theta}(V_\theta e^{z}\sin\theta)-2V_r e^{z}\sin\theta\right] \quad (6)$$

(c) Polar momentum

$$\sigma=V_\theta;\quad \Gamma_z=\Gamma_\theta=1/Gr^{1/2}$$
$$\delta_{\text{source}}=-V_rV_\theta e^{2z}\sin\theta-e^{2z}\sin\theta\frac{\partial p_d}{\partial\theta}+\xi e^{3z}\sin^2\theta+\frac{1}{Gr^{\frac{1}{2}}}\left[2e^{z}\sin\theta\frac{\partial V_r}{\partial\theta}-\frac{V_\theta e^{z}}{\sin\theta}\right] \quad (7)$$

(d) Energy equation

$$\sigma=\xi;\quad \Gamma_z=\Gamma_\theta=1/(PrGr^{1/2});\quad \delta_{\text{source}}=0 \quad (8)$$

At time $t'=0$ the fluid surrounding the sphere is at rest. Thus, the initial conditions are given by $V_\theta=V_r=\xi=p_d=0$ for $z>0$ and $0<\theta<\pi$. At the sphere surface ($z=0$), both the initial and the boundary conditions are given as $V_\theta=V_r=0$ and $\xi=1$.

Boundary conditions on the axis of symmetry, where $\theta=0$, π, is given by

$$V_\theta=\partial V_r/\partial\theta=\partial\xi/\partial\theta=\partial p_d/\partial\theta=0$$

On the outer boundary ($z=z_\infty$), boundary conditions suitable for having mass and energy transfer across the boundary is employed. Thus,

$$\frac{\partial}{\partial z}(V_re^{2z})=p_d=V_\theta=0$$

(a) At the inflow region ($V_r<0$), $\xi=0$.
(b) At the outflow region ($V_r>0$), $\partial\xi/\partial z=0$.

The pressure and viscous drag coefficients are given as

$$C_{D,p}=2\int_0^\pi p_d|_s\sin2\theta\,d\theta \quad (9)$$

and

$$C_{D,\mu}=-\frac{4}{Gr^{\frac{1}{2}}}\int_0^\pi\left.\frac{\partial V_\theta}{\partial z}\right|_s\sin^2\theta\,d\theta \quad (10)$$

The total drag coefficient is given by

$$C_D=C_{D,p}+C_{D,\mu} \quad (11)$$

The local and the overall Nusselt numbers are expressed as

$$Nu_\theta=\frac{h'_\theta(2R'_0)}{k'}=\frac{(2R'_0)\left(\frac{\partial T}{\partial r'}\right)_s}{T_s-T_\infty}=-2\left(\frac{\partial\xi}{\partial z}\right)_s \quad (12a)$$

and

$$Nu=\frac{\bar{h}'(2R'_0)}{k'}=-\int_0^\pi\left.\frac{\partial\xi}{\partial z}\right|_{z=0}\sin\theta\,d\theta \quad (12b)$$

where the average heat transfer coefficient $\bar{h}'$ is computed using the expression given below.

$$\bar{h}'(T_s-T_\infty)(4\pi R'^2_0)=-\int_0^\pi\left(k'\frac{\partial T}{\partial r'}\right)_s 2\pi R'_0\sin\theta R'_0\,d\theta \quad (12c)$$

3. Numerical method

The governing equations are discretized using the finite control volume formulation and the hybrid scheme (Patankar, 1980). A staggered grid is employed for the velocity components. As mentioned earlier, $z=0$ indicates the sphere surface and $z=z_\infty$ indicates the "computational infinity". This is an approximation which causes negligible error in heat transfer and stress distribution near the sphere surface when z_∞ is adequately large. The velocity components, temperature and motion pressure from the previous time step have been used to evaluate the coefficients and source term in the algebraic equations. The SIMPLEC algorithm developed by Van Doormaal and Raithby (1984) has been employed to evaluate the motion pressure field. The equations are solved by the ADI (Alternating Direction Implicit) method. The modified TDMA (Tri Diagonal Matrix Algorithm) solver with a relaxation parameter of 1.85 (Van Doormaal and Raithby, 1984) was used along each of the two alternating directions and the solution is obtained through iterations within a time step. For an indication of convergence in the iteration process, an average Euclidean norm has been calculated and the convergence is determined by checking whether the norm after certain number of iterations is less than or equal to the product of the average norm of the first iteration and a residual reduction factor. The residual reduction factor is taken as 0.1 for velocities and temperature, and 0.2 for pressure correction as recommended by Van Doormaal and Raithby (1984). Extensive simulations have been carried out to select the appropriate numerical parameters. Thus, the parameters listed in Table 1 ensure that the final solutions are reasonably independent of grid size (Δz and $\Delta\theta$), time increment (Δt), and "computational infinity" ($r_\infty=e^{z_\infty}$). For example, results presented in Table 2 show

Table 1
Numerical parameters used in the present study

Gr	Parameter	Pr			
		0.02	0.7	7	100
10^5	Δz	0.02	0.01	0.005	0.005
	$\Delta\theta$	2°	1°	1°	1°
	Δt	0.08	0.05	0.05	0.05
	r_∞	54	20	20	11
10^6	Δz	0.02	0.01	0.005	0.003
	$\Delta\theta$	2°	1°	0.5°	0.5°
	Δt	0.08	0.05	0.03	0.03
	r_∞	54	20	20	11
10^7	Δz	0.01	0.005	0.0025	0.0025
	$\Delta\theta$	1°	0.5°	0.5°	0.5°
	Δt	0.05	0.03	0.03	0.03
	r_∞	20	12	7.4	7
10^8	Δz	0.005	0.0025	0.0025	0.0015
	$\Delta\theta$	1°	0.5°	0.5°	0.5°
	Δt	0.03	0.03	0.03	0.03
	r_∞	20	7.4	7.4	7
10^9	Δz	0.003	0.0025	0.0015	0.001
	$\Delta\theta$	0.5°	0.5°	0.5°	0.5°
	Δt	0.02	0.02	0.02	0.02
	r_∞	11	7.4	5.2	5.2

Table 2
Effect of computational infinity on "steady-state" drag coefficients and overall Nusselt number for $Gr = 10^6$ and $Pr = 0.02$

r_∞	$C_{D,p}$	$C_{D,\mu}$	Nu
20	6.086	9.400	0.5611
54	6.121	9.438	0.5610
120	6.120	9.437	0.5610

how the value of r_∞ was selected as 54 for the case of $Gr = 10^6$ and $Pr = 0.02$ (Table 1). To better explain the procedure for the selection of grid size, time step and computational infinity, a typical case of $Gr = 10^6$ and $Pr = 0.02$ has been considered and the details are presented in Appendix A.

4. Results and discussion

4.1. Validation

The numerical model has been validated with the experimental results available in the literature. An experimental investigation of free convection heat transfer from heated spheres to water has been reported by Amato and Tien (1972). A case where the Rayleigh number (Ra_D) is equal to 1.7×10^8, has been simulated and the variations of the temperature with the normal (radial) distance, at different angles have been compared with the experimental results reported in (Amato and Tien, 1972). Fig. 2 shows the non-dimensional temperature profiles obtained from the present study in comparison with those measured by experiments (Amato and Tien, 1972). It is clear from Fig. 2 that the numerical model is able to predict the temperature variations very close to those measured in

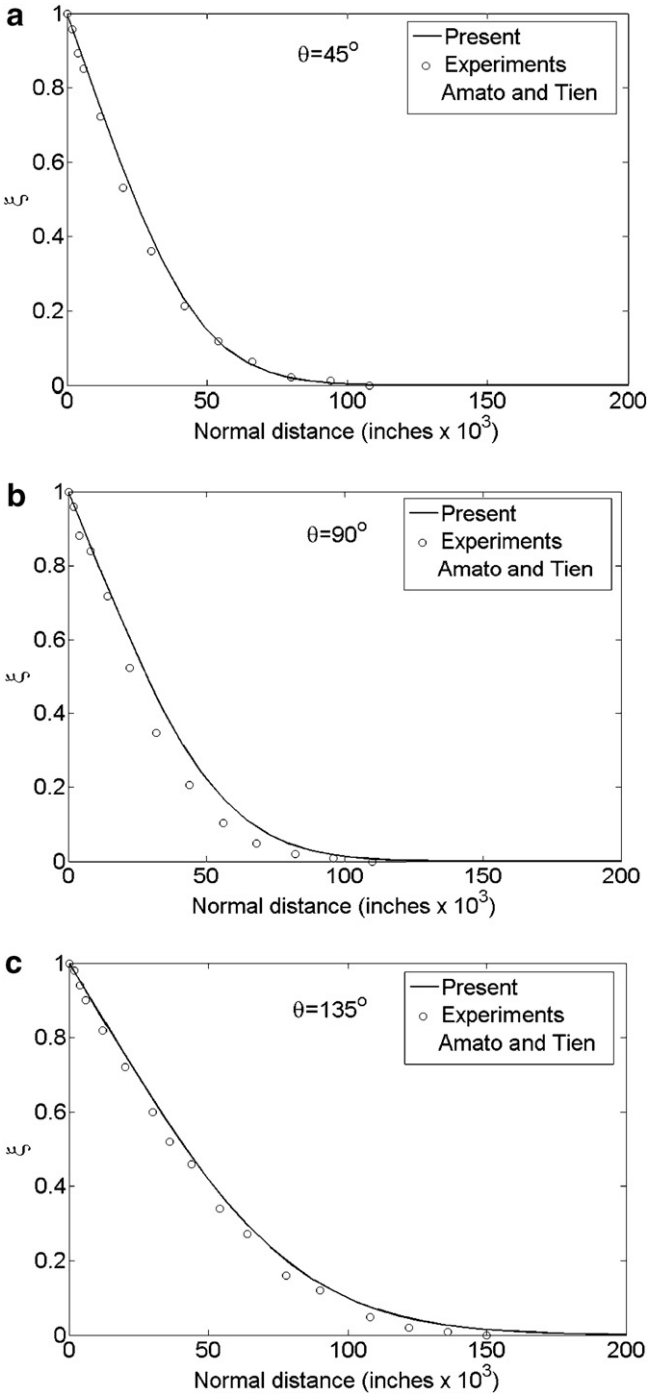

Fig. 2. Non-dimensional temperature profiles at different angles ($Ra_D = 1.7 \times 10^8$).

the experiments. For the same case, the variation of velocity with the normal distance obtained from both numerical model as well as the experiments has been plotted in Fig. 3. Near the sphere surface, the velocity profiles between the numerical model and experiments agree well. However, the numerical model slightly over-predicts the velocity values at larger normal distances. The reasons for this may be multifold; the assumptions in the numerical model, such as axisymmetric and laminar flow, errors due to the

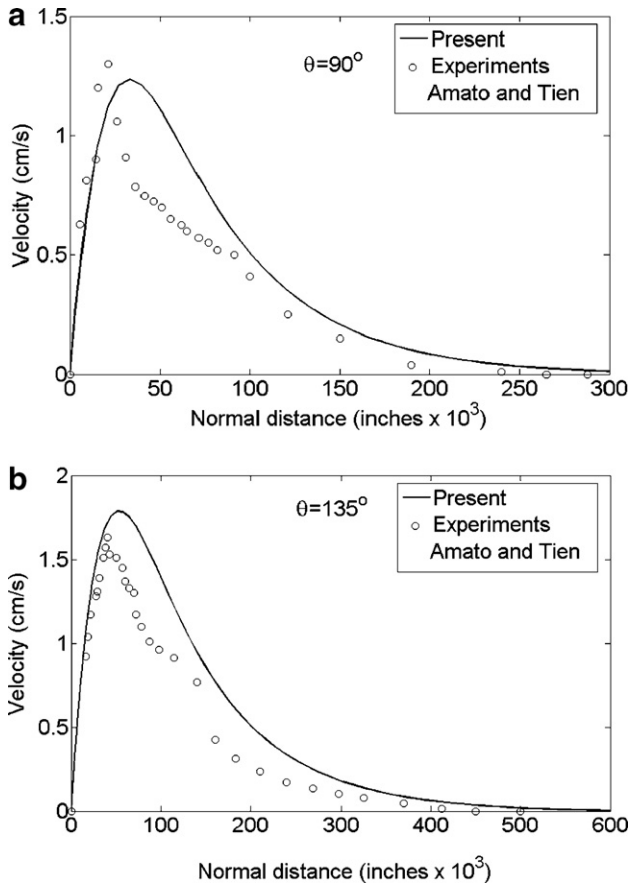

Fig. 3. Velocity profiles at different angles ($Ra_D = 1.7 \times 10^8$).

interference of the velocity measuring probe and the presence of velocity fluctuations in the experimental measurements, could be some of these reasons.

To further validate the code, the overall Nusselt numbers (Nu) and the total drag coefficients (C_D) have been compared with the results obtained by Jia and Gogos (1996a), where a stream function-vorticity formulation has been adopted. Table 3 shows that the maximum variations in Nu and C_D between the present results and those reported in Jia and Gogos (1996a) are around 5.5% and 7%, respectively. As mentioned earlier, the present model allows for the inflow in the lower part of the outer boundary and outflow in the upper part. The model reported in (Jia and Gogos, 1996a) considered no cross flow at the outer boundary, which may be the reason for such variation between the results presented in Table 3. Dudek et al. (1988) employed the same boundary condition as in the present model. In order to compare the results of the present work with those reported by Dudek et al. (1988), a simulation was conducted for small Grashof number ($Gr = 0.05$) and $Pr = 0.72$. Table 4 presents Nu and C_D values from (Dudek et al., 1988) and the present work. The maximum difference between the results for both quantities is less than 2%.

Table 3
"Steady-state" overall Nu and C_D for $Pr = 0.7$ and various Grashof numbers

	Grashof number					
	10^5		10^6		10^7	
	Nu	C_D	Nu	C_D	Nu	C_D
Present	27.86	0.357	48.11	0.200	84.12	0.113
Jia and Gogos (1996a)	28.74	0.36	49.85	0.190	89.62	0.105

Table 4
"Steady-state" overall Nu and C_D for $Gr = 0.05$ and $Pr = 0.72$

Results of	C_D	Overall Nusselt number
Present model	4.26	2.14
Dudek et al. (1988)	4.33	2.13

4.2. Transient temperature and flow fields

In Fig. 4, the temporal evolution (with respect to the dimensionless time) of temperature contours has been presented for $Gr = 10^8$ and different Prandtl numbers. Initially, convection effects are very weak and conductive heat transfer is predominant. Consequently, the temperature contours are nearly symmetric in the radial direction ($t = 1.2$ in Fig. 4). As time proceeds, the buoyancy-induced motion increases gradually and a transient plume with a mushroom-shaped cap forms above the sphere ($t = 3.6$ in Fig. 4). This is consistent with the observations available in the literature (Shlien and Boxman, 1980). Eventually, the stem of the plume becomes steady, whereas the plume cap rises continuously and eventually "flows out" of the computational domain ($t = 8.4$ and 24 in Fig. 4). The thicknesses of the transient cap and of the steady plume stem decreases with increasing Prandtl number. In Fig. 5, the temporal evolution (with respect to the dimensionless time) of the streamlines is presented for the same set of Prandtl number and Grashof numbers as in Fig. 4. The entrained fluid rises and then rolls downward resulting in a velocity pattern in the form of a vortex ring, initially located at the side of the sphere ($t = 1.2$ in Fig. 5). As time progresses, the vortex ring is pushed upward along the surface of the sphere ($t = 3.6$, 6 and 8.4 in Fig. 5). After it reaches the top of the sphere, it sheds out of the computational domain ($t = 24$ in Fig. 5). It can be noted that the upward movement of the vortex ring is slowed down with increasing Prandtl number.

The temporal evolution of temperature contours and streamlines for $Pr = 7$ and different Grashof numbers are presented in Figs. 6 and 7, respectively. In this case, in the temperature contours, the thicknesses of both the transient cap and the steady plume stem decreases with increasing Grashof number (Fig. 6). As far as the streamlines are concerned, the upward movement of the of vortex ring with dimensionless time does not seem to be affected by the increasing value of the Grashof number (Fig. 7). That is, irrespective of the Grashof number value, at the same dimensionless time, the vortex ring reaches the upper part

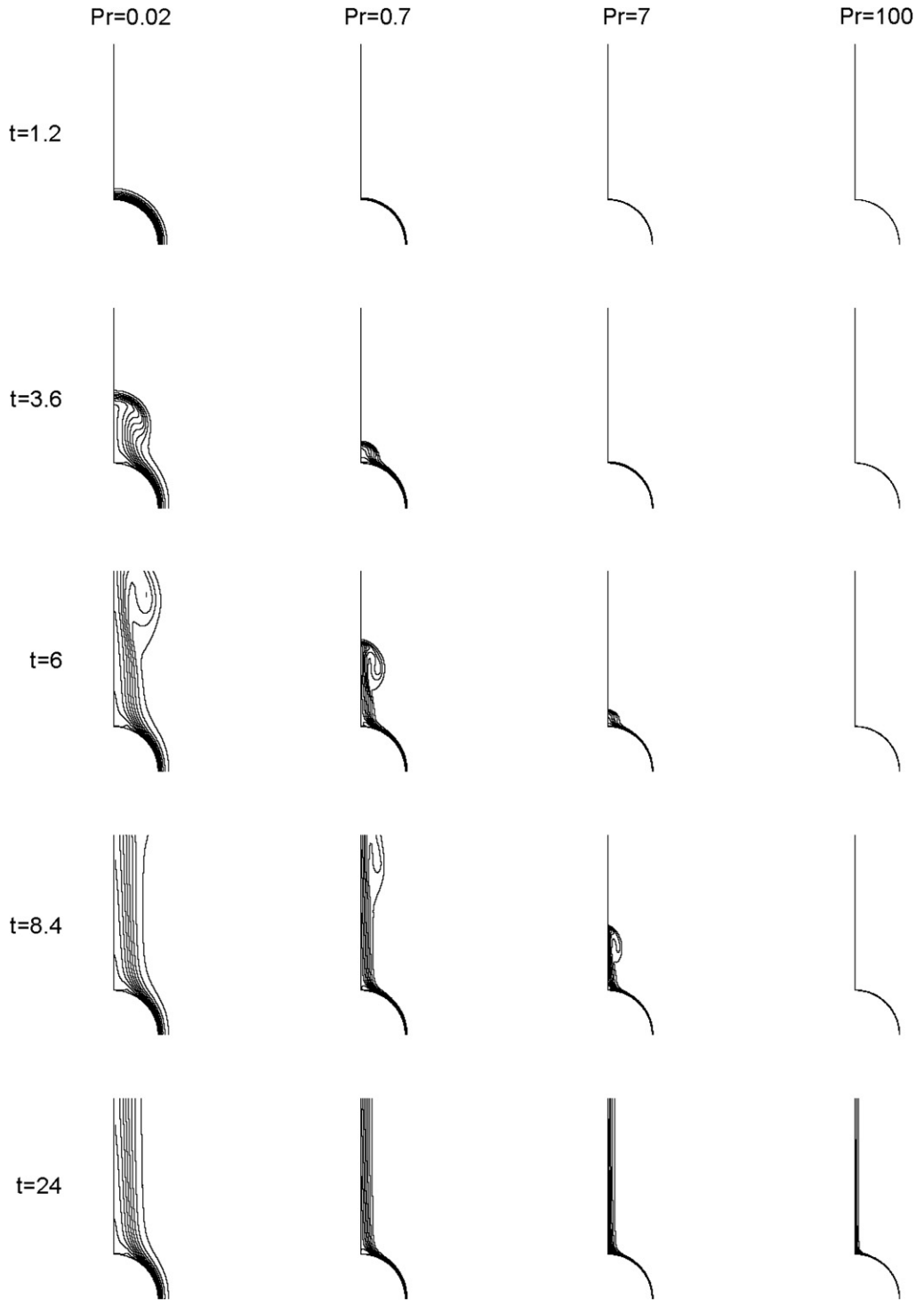

Fig. 4. Non-dimensional temperature (ξ) contours for $Gr = 10^8$ and different Prandtl numbers at different non-dimensional times ($\xi_{min} = 0.05$, $\xi_{max} = 0.95$ and $\Delta\xi = 0.15$).

of the computational domain and it is shed out, unlike the previous case, where the increasing Prandtl number slowed down the upward movement of the vortex ring (Fig. 5). However, it should be noted that since, the dimensionless time is proportional to the square root of the Grashof number, this implies that with respect to the dimensional time, both the plume cap (Fig. 6) and the vortex ring (Fig. 7) move upward faster with increasing Grashof number.

4.3. Recirculation vortex

Jia and Gogos (1996a,b) reported that a recirculation vortex forms in the wake of the sphere for high Grashof

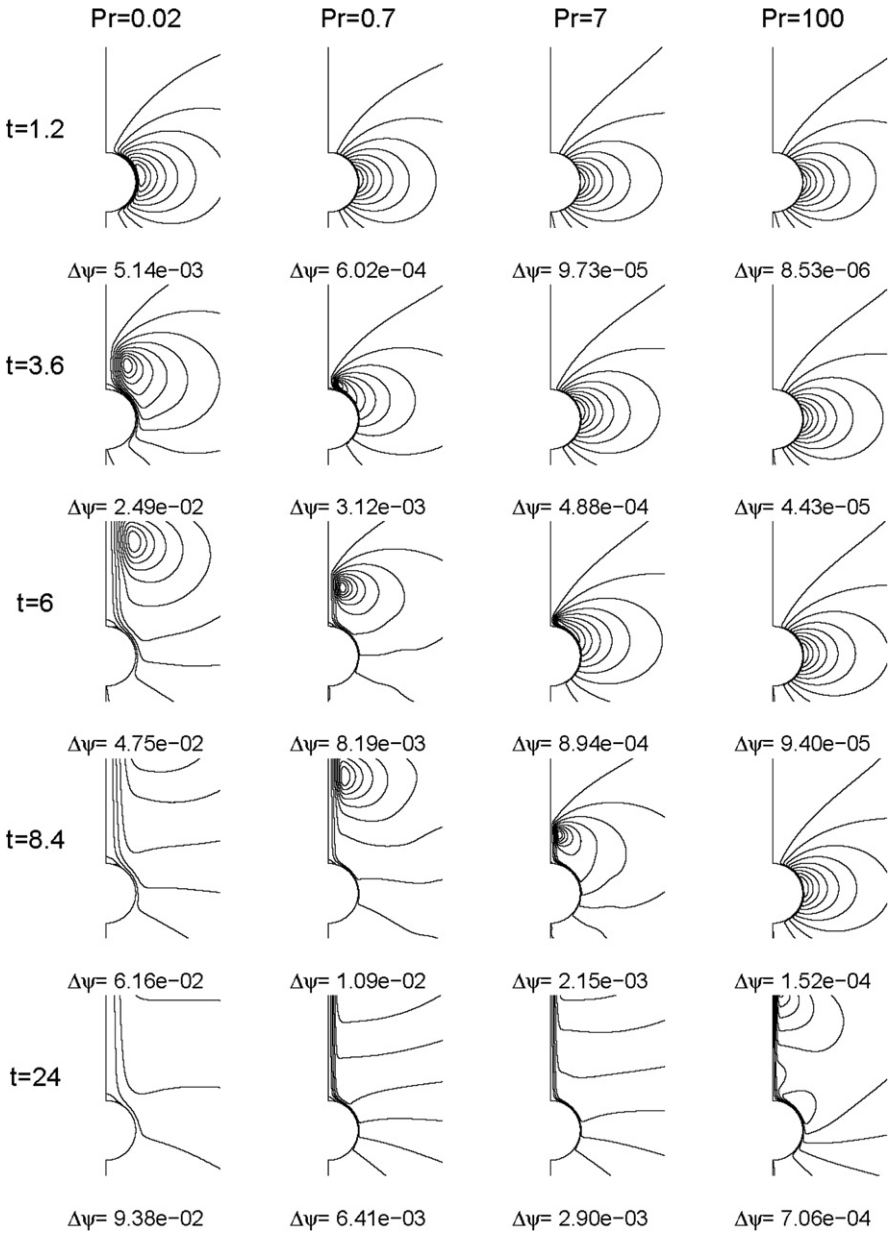

Fig. 5. Streamlines for $Gr = 10^8$ and different Prandtl numbers at different non-dimensional times ($\psi_{min} = 0$).

number ($Gr \geqslant 10^7$) and $Pr = 0.72$. No vortex was found for ($Pr = 7$) in their numerical study. In the present study, a range of higher Grashof number ($10^5 \leqslant Gr \leqslant 10^9$) and a wider range of Prandtl numbers ($Pr = 0.02$, 0.7, 7 and 100) have been investigated. For adequately large Grashof number, a recirculation vortex has been observed for $Pr = 0.02$, 0.7 and 7. The presence of the recirculation vortex depends not only on the Grashof number but also on the Prandtl number. In general, the shape of the vortex is similar to that reported by Jia and Gogos (1996a,b), that is, the vortex resembles a small thin cap which is located very close to the top surface of the sphere and next to the axis of symmetry. Typically, the angular extent is larger than its radial dimension.

Fig. 8 presents the "steady-state" streamlines in the wake of the sphere for $Pr = 0.02$, 0.7 and 7 and different Grashof numbers. Jia and Gogos (1996a) concluded that the size of the vortex increases with Grashof number. Although such a statement is valid for $Pr = 0.72$, considered in their study, the present study, which includes a wider range of Prandtl numbers indicates a more complex dependence of the vortex size on Grashof and Prandtl numbers. Thus, for the lowest Pr considered ($Pr = 0.02$), the vortex's radial extent decreases slightly with Grashof number. Furthermore, the higher the Prandtl number, the higher the Grashof number at which a vortex is present. The size of the vortex, both in its axial and angular extent, decreases with increasing Prandtl number (Fig. 8). Also, no

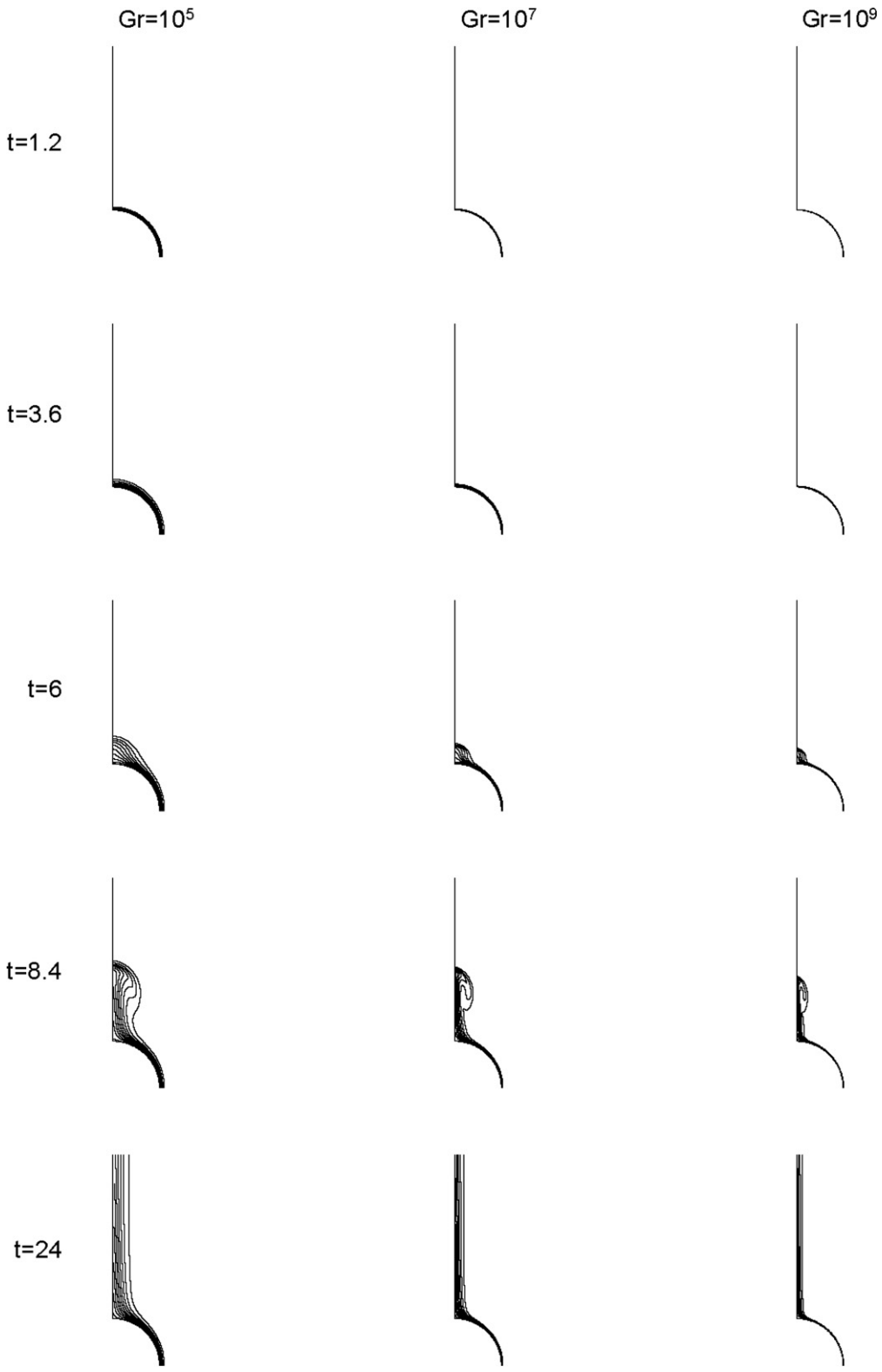

Fig. 6. Non-dimensional temperature (ξ) contours for $Pr = 7$ and different Grashof numbers at different non-dimensional times ($\xi_{min} = 0.05$, $\xi_{max} = 0.95$ and $\Delta\xi = 0.15$).

vortex was observed for $Pr = 100$ in the range of Grashof numbers investigated. In Fig. 9, non-dimensional temperature contours (on the left) and streamlines (on the right) near the top of the sphere are presented for $Gr = 10^7$ and $Pr = 0.02$ at different non-dimensional times. The vortex evolves with time as seen in Fig. 9. At approximately $t = 2.4$, a thin vortex appears with an angular extent of approximately $\pi/6$. The vortex grows in the radial

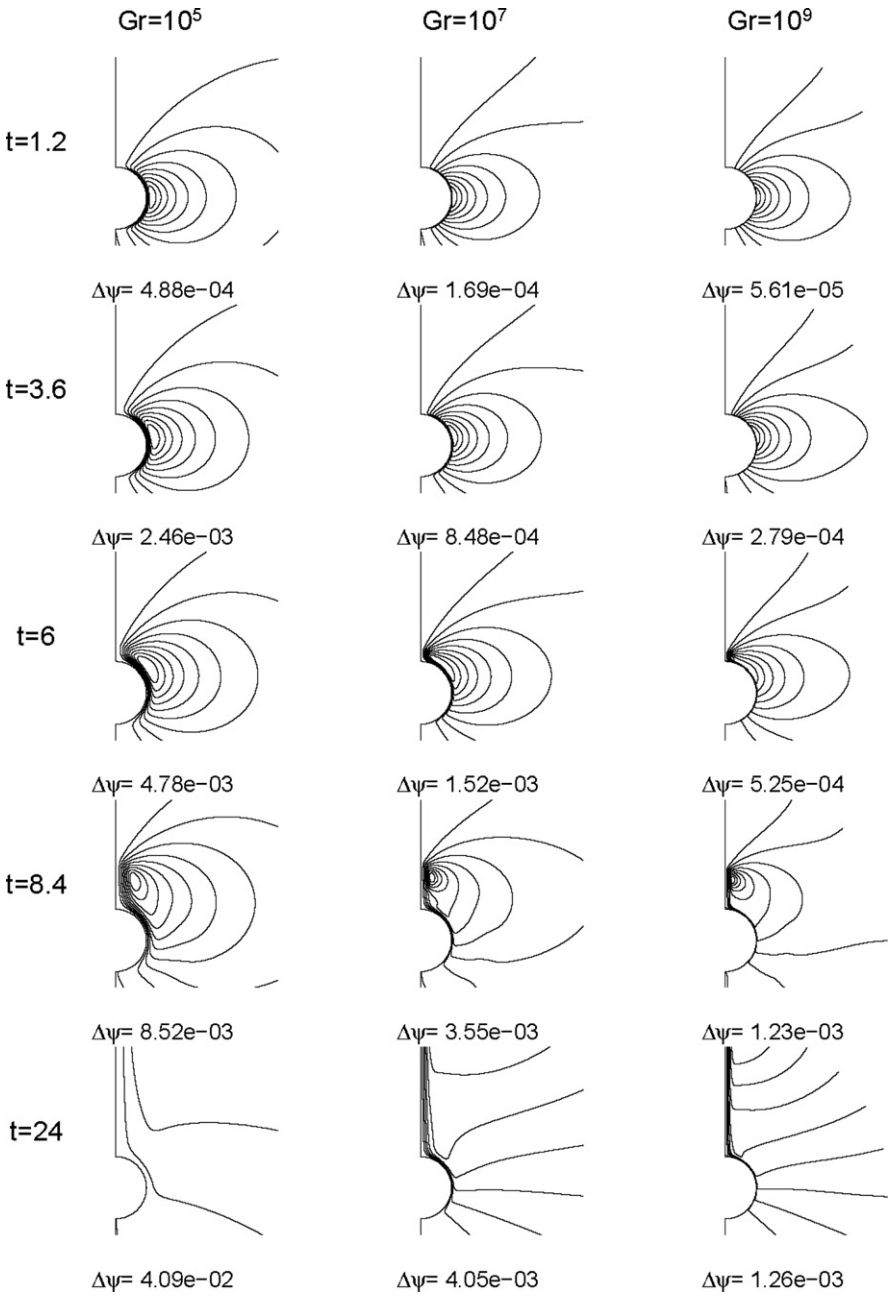

Fig. 7. Streamlines for $Pr = 7$ and different Grashof numbers at different non-dimensional times ($\psi_{\min} = 0$).

direction with time while its angular extent remains constant. The presence of the vortex drastically alters the temperature distribution near the top of the sphere as seen in Fig. 9.

4.4. Transverse velocity and temperature profiles

Fig. 10 presents the "steady-state" vertical velocity component V_Y along the transverse axis X ($X = X'/R'_0$) in the vicinity of the top of the sphere for $Pr = 0.02$ and $Gr = 10^8$. Close to the sphere surface ($Y = Y'/R'_0 = 1.1$) the vertical velocity component around the axis of symmetry is negative due to flow reversal (vortex) on the top of the sphere. Above the flow reversal region (wake), the velocity along the centerline ($X = 0$) increases with increasing distance (Y) from the sphere surface. The temperature profiles for the same locations corresponding to Fig. 10 are shown in Fig. 11. At ($Y = 1.1$), the peak of the temperature is set off from the axis of symmetry due to the presence of the vortex. The vertical velocity component V_Y and temperature profiles along the transverse axis in the vicinity of the top of the sphere are shown in Figs. 12 and 13 for $Pr = 7$ and $Gr = 10^8$. Due to the absence of the vortex near the top of the sphere for this case, the vertical velocity is always positive. The extent of the velocity profile with X decreases with increasing Y till $Y < 2$ and then increases with increasing Y for $Y > 2$ (Fig. 12). This is consistent with the observations of Jaluria and Gebhart (1975).

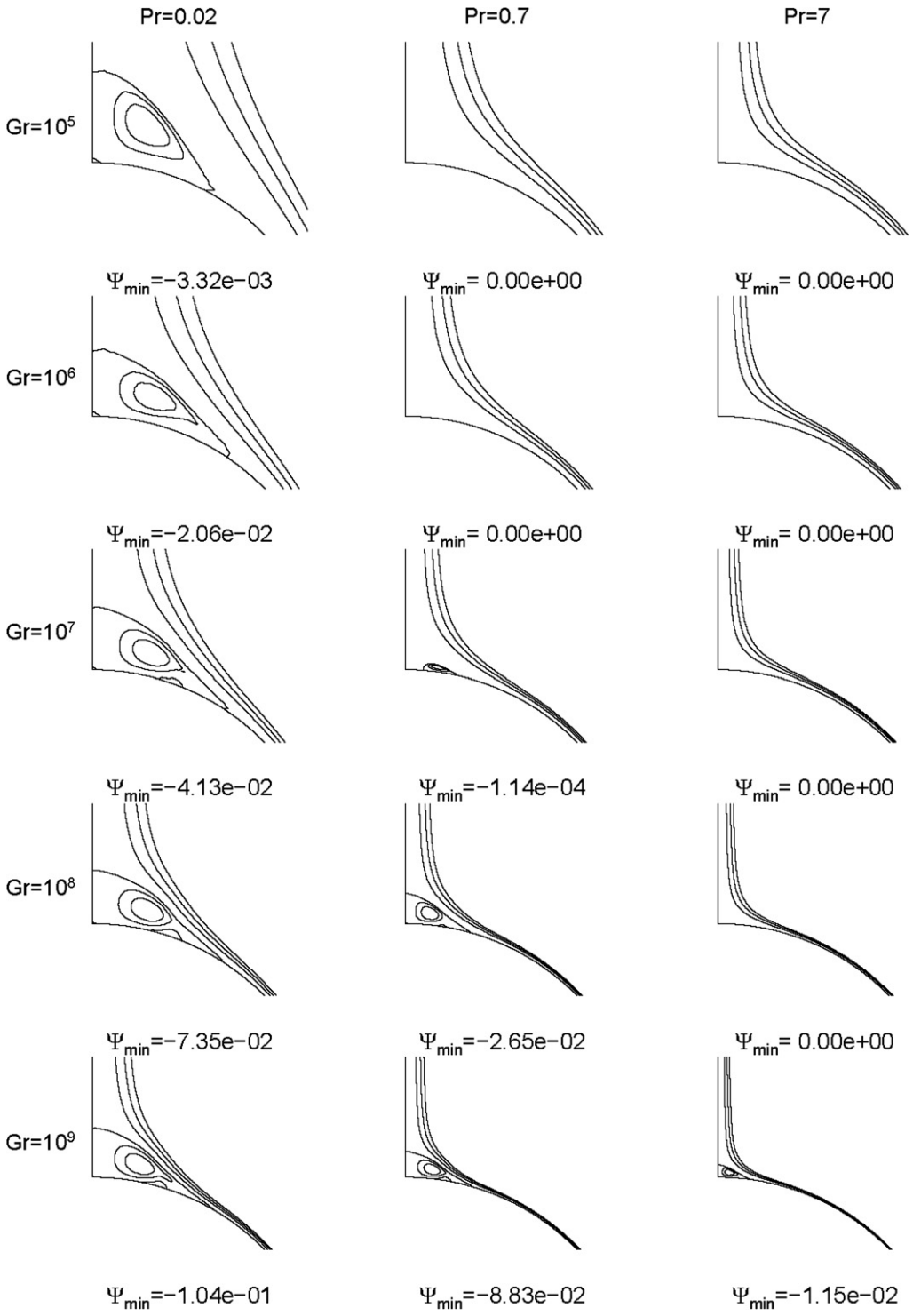

Fig. 8. "Steady-state" streamlines in the wake of the sphere for $Pr = 0.02$, 0.7 and 7 and different Grashof numbers. $\Psi = Gr^{1/4}Pr^{1/2}\psi$. Vortex ($\Psi < 0$): $\Delta\Psi = 1/2\Psi$. For $\Psi > 0$: $\Psi = 0.15$, 0.3, 0.45.

4.5. Overall Nusselt number and total drag coefficients

The temporal evolution of the total drag coefficient and the overall Nusselt number for $Gr = 10^8$ and different Prandtl numbers are shown in Figs. 14 and 15. At low Prandtl numbers ($Pr = 0.02$, 0.7 and 7), the total drag coefficient increases to a maximum value before reaching the "steady-state" value. This trend has been reported in the literature (Jia and Gogos, 1996a). However, for $Pr = 100$, the total drag coefficient gradually increases and reaches

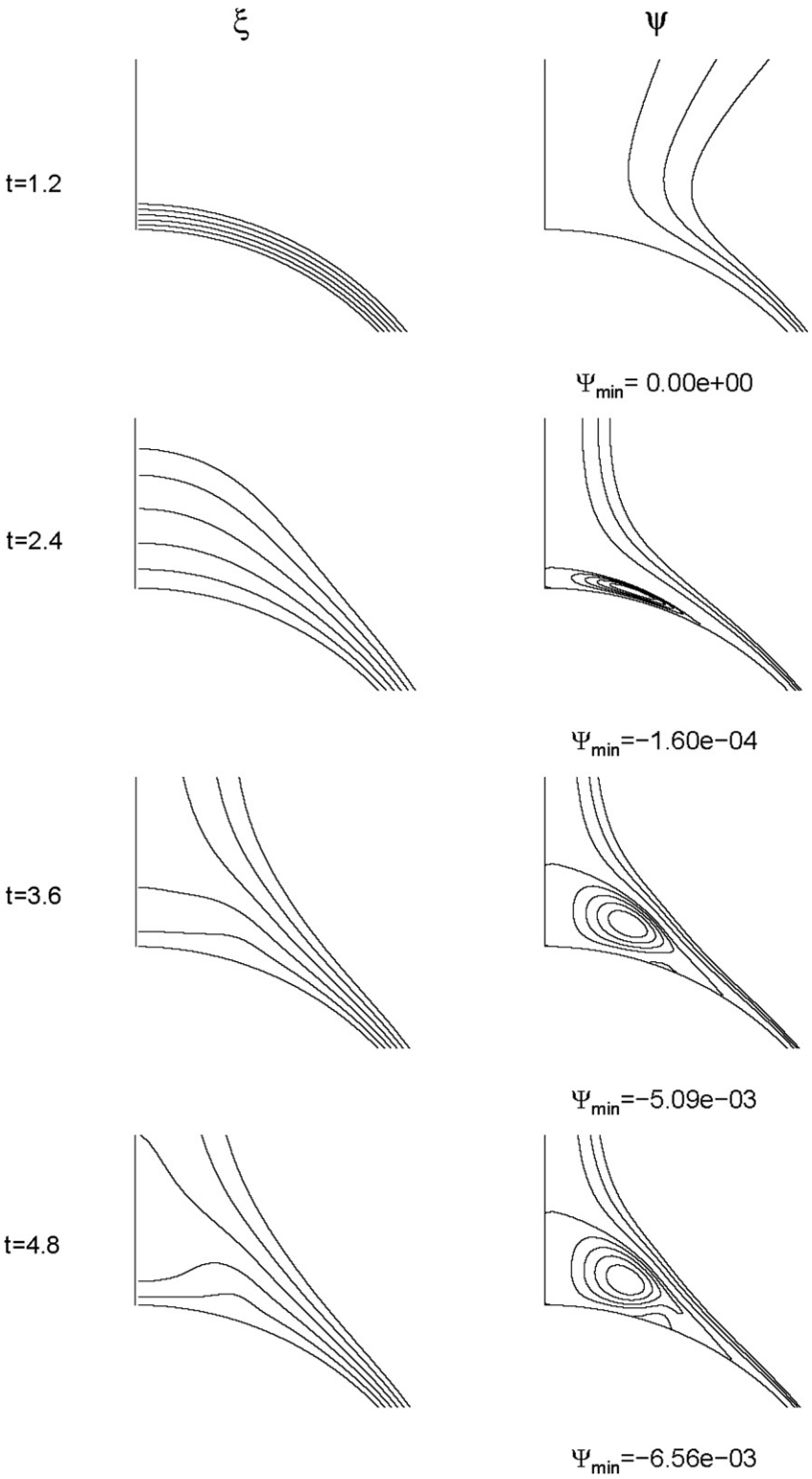

Fig. 9. "Steady-state" non-dimensional temperature contours (left) and streamlines (right) in the wake of the sphere for $Pr = 0.02$ and $Gr = 10^7$ at different times. Temperature: $\xi_{min} = 0.75$, $\xi_{max} = 1$ and $\Delta\xi = 0.05$; Streamline: $\Delta\psi = 1/4\psi_{min}$ for vortex and $\psi = 0.005$, 0.01 and 0.015 for $\psi > 0$.

the "steady-state" value (Fig. 14). The larger viscous effects associated with $Pr = 100$, may be the cause for such slow evolution of the total drag coefficient. Similarly, at low Prandtl numbers ($Pr = 0.02$, 0.7 and 7), the overall Nusselt number reaches a minimum, before reaching the "steady-state" value and at $Pr = 100$, Nu gradually decreases to

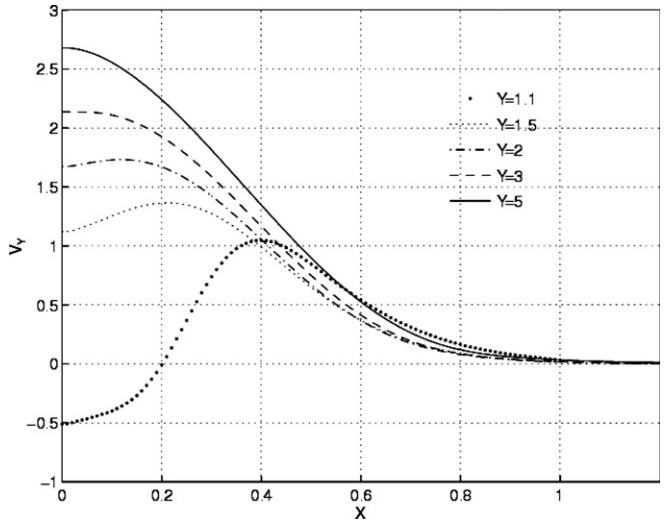

Fig. 10. "Steady-state" vertical velocity in the wake of the sphere for $Pr = 0.02$ and $Gr = 10^8$.

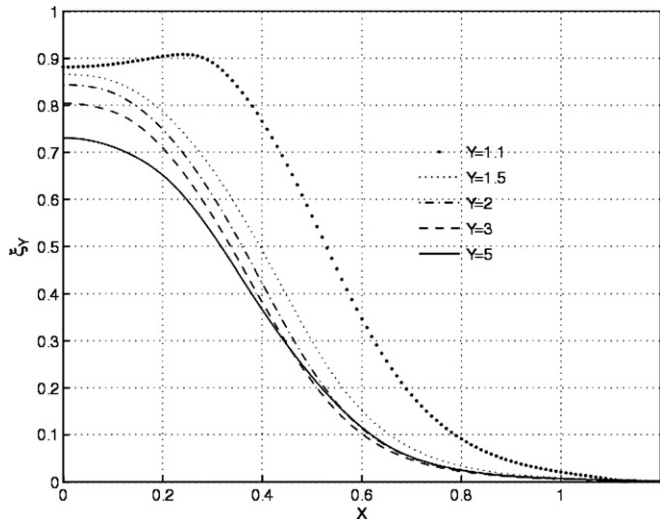

Fig. 11. "Steady-state" temperature profiles in the wake of the sphere for $Pr = 0.02$ and $Gr = 10^8$.

the "steady-state" value (Fig. 15). It can be observed from Figs. 14 and 15 that as Pr increases, time to reach the "steady-state" also increases.

Fig. 16 presents the overall Nusselt number as a function of Rayleigh number ($Ra_D = Gr_D Pr$) for $Pr = 0.02$, 0.7, 7 and 100. The results obtained from the present study are indicated by symbols. The results from the correlation presented by Churchill (1983) are shown by dashed lines. The solid line represents the result obtained from Churchill's correlation for $Pr \to \infty$. The present results are in very good agreement with the correlation (Churchill, 1983).

The total drag coefficient as a function of the square root of the Grashof number is presented in Fig. 17. Dashed lines show the analytical solution reported by Stewart

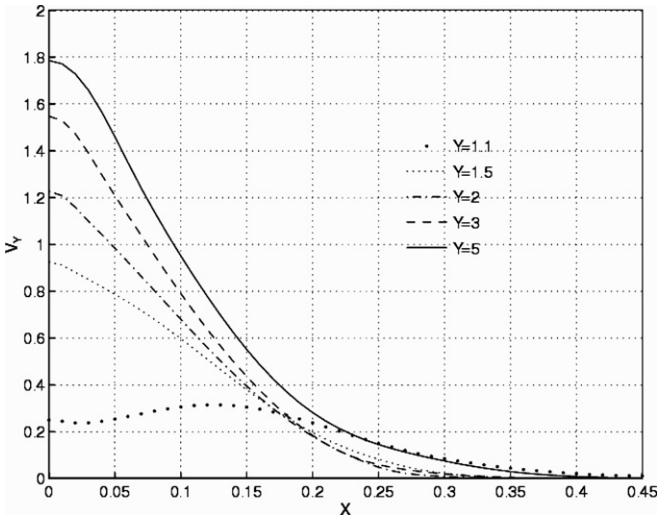

Fig. 12. "Steady-state" vertical velocity in the wake of the sphere for $Pr = 7$ and $Gr = 10^8$.

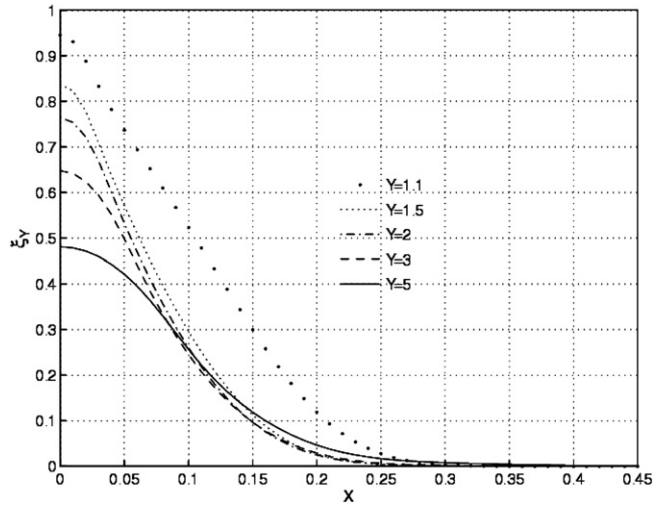

Fig. 13. "Steady-state" temperature profiles in the wake of the sphere for $Pr = 7$ and $Gr = 10^8$.

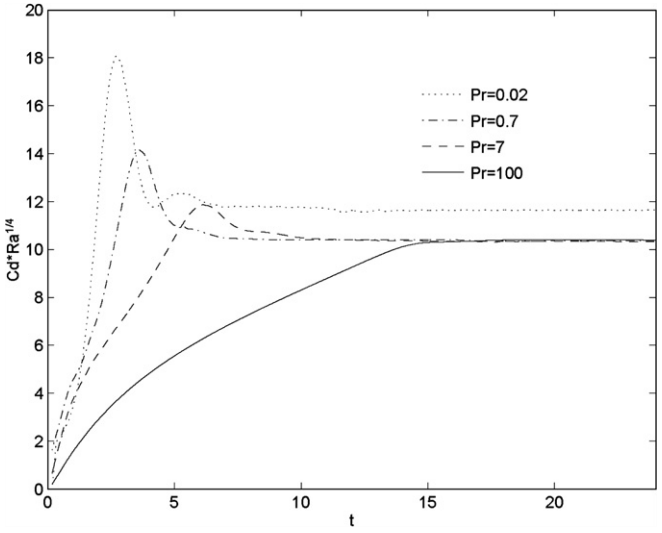

Fig. 14. Temporal evolution of the total drag coefficient as a function of Prandtl number for $Gr = 10^8$.

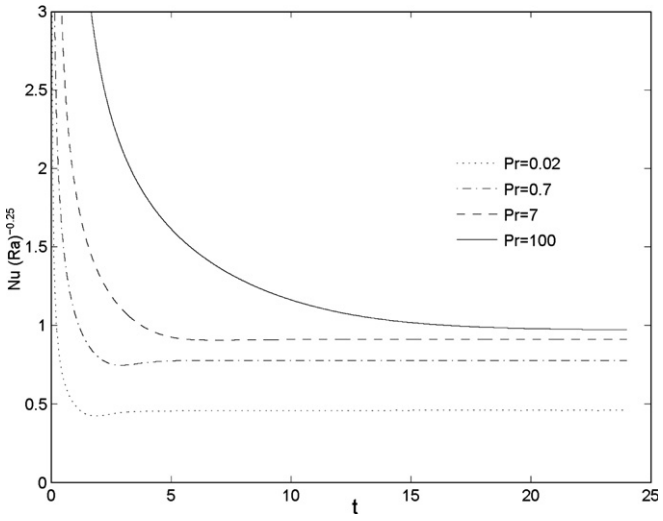

Fig. 15. Temporal evolution of the overall Nusselt number as a function of Prandtl number for $Gr = 10^8$.

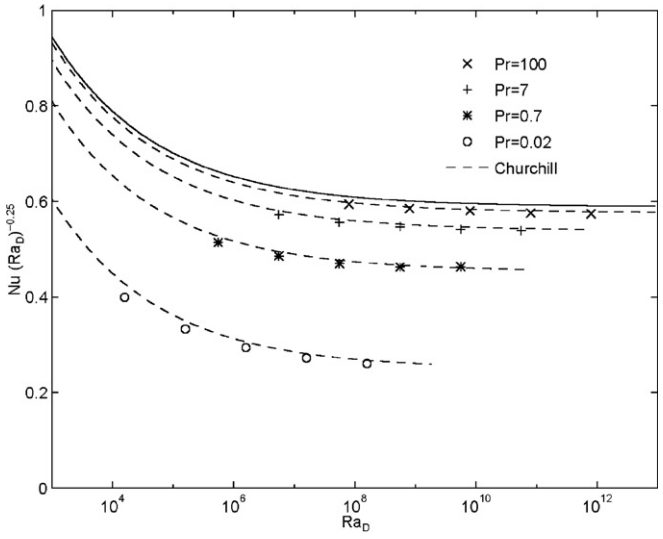

Fig. 16. "Steady-state" overall Nusselt number as a function of Ra_D.

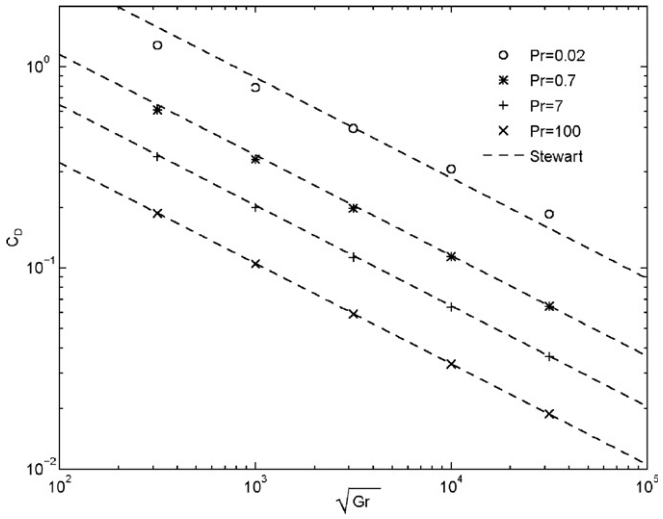

Fig. 17. "Steady-state" total drag coefficient as a function of $Gr^{1/2}$.

(1971), which is based on boundary layer theory for low Prandtl numbers and an asymptotic series expansion for large Prandtl numbers. At low Prandtl numbers, the results from the present study deviate from those reported in Stewart (1971). This may be due to the fact that the boundary layer solution was employed for the low Prandtl number cases. However, at a larger Prandtl number ($Pr = 100$), results from the present study closely agree with the results presented in (Stewart, 1971). The asymptotic series expansion employed at larger Pr may be the reason for this.

5. Summary

The full Navier–Stokes equations and energy equation for laminar natural convection heat transfer over an isothermal sphere were discretized using the finite control volume formulation and were solved by employing the SIMPLEC method. At the outer boundary of the computational domain, boundary conditions suitable for having mass and energy transfer across the boundary have been employed. Transient and "steady-state" results were obtained for a wide range of high Grashof numbers ($10^5 \leqslant Gr \leqslant 10^9$) and a wide range of Prandtl numbers ($Pr = 0.02$, 0.7, 7 and 100). The main results are summarized below.

When an isothermal sphere is placed within a cold ambient fluid, conductive heat transfer is initially predominant. As time advances, an axisymmetric plume with a mushroom-shaped cap forms near to the top of the sphere and the plume cap moves upward due to the buoyancy-induced flow-field. The upward movement of the plume cap is slowed as the Prandtl number increases. The size and the level of temperature of the transient cap and plume stem decrease with increasing Gr and Pr. As the plume cap moves upward, the temperature and flow field around the sphere gradually reaches a "steady-state" condition. The time at which the "steady-state" is reached, increases with the Prandtl number. The presence of a vortex in the wake of the sphere has been predicted and has been clearly delineated as a function of both Grashof and Prandtl numbers. For low Prandtl number cases ($Pr = 0.02$, 0.7 and 7), temporal evolution of the overall Nusselt numbers and the total drag coefficients show that the overall Nusselt number and the total drag coefficient reach a local minimum and a local maximum value, respectively, before reaching the "steady-state." At $Pr = 100$, the overall Nusselt number and the total drag coefficient reach the "steady-state" value monotonically. The overall Nusselt numbers and total drag coefficients for the range of Grashof and Prandtl numbers investigated are presented and they are in very good agreement with studies available in the literature.

Acknowledgements

This research was funded by ARO EPSCoR under Grant DAAD19-99-1-0116. Computational resources were provided by the Thermal/Fluids Computational Facility

and the Research Computing Facility at the University of Nebraska—Lincoln.

Appendix A

The case where $Gr = 10^6$ and $Pr = 0.02$ has been considered throughout this section. The influence of the radial increment (Δz) has been tested by considering 3 values for Δz and studying its impact on the variation of non-dimensional temperature with normal distance at $\theta = 45°$. Fig. A1 shows that the profiles compare very closely between the cases of $\Delta z = 0.01$ and $\Delta z = 0.02$, implying that $\Delta z = 0.02$ would be accurate for the set of Gr and Pr considered. The influence of the tangential increment ($\Delta\theta$) has been tested by considering 3 values for $\Delta\theta$ and studying its impact on the variation of surface pressure (non-dimensional) along the surface of the sphere. Fig. A2 shows that the pressure variation along the sphere

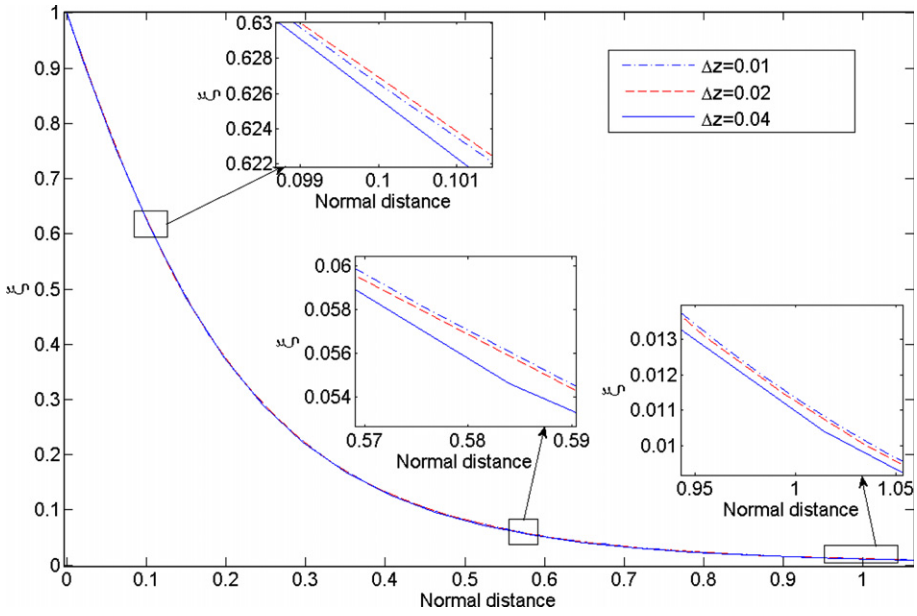

Fig. A1. Non-dimensional temperature vs. normal distance for different Δz values ($\Delta t = 0.08$, $\Delta\theta = 2°$ and $r_\infty = 54$).

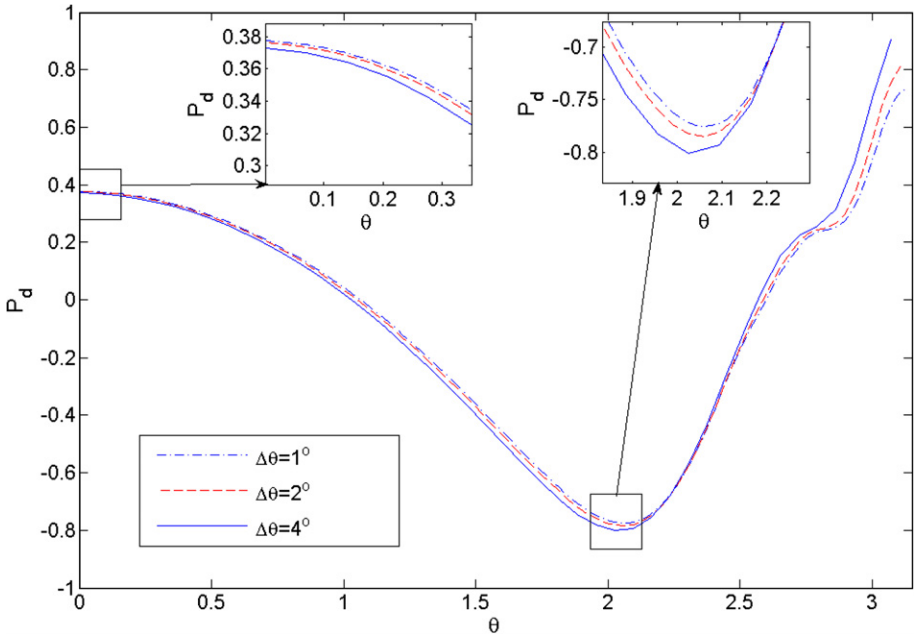

Fig. A2. Non-dimensional surface pressure along sphere surface for different $\Delta\theta$ values ($\Delta z = 0.02$, $\Delta t = 0.08$ and $r_\infty = 54$).

surface compares closely between the cases of $\Delta\theta = 1°$ and $\Delta\theta = 2°$. Thus, $\Delta\theta = 2°$ would be accurate for the set of Gr and Pr considered. The influence of the computational infinity (r_∞) has been tested by considering 3 values for r_∞ and studying its impact on the variation of radial velocity (cm/s) with the normal distance at $\theta = 45°$. Fig. A3 shows that the variation of radial velocity (cm/s) with the normal distance compares closely between the cases of $r_\infty = 54$ and $r_\infty = 108$, thus, $r_\infty = 54$ would be accurate for the set of Gr and Pr considered. Finally, the influence of the time step has been tested by considering 3 values for Δt and studying its impact on the variation of the overall drag coefficient with time. Fig. A4 shows that the temporal variation of the overall drag coefficient compares closely between the cases of $\Delta t = 0.08$ and $\Delta t = 0.04$. This shows that $\Delta t = 0.08$ would be accurate enough for the set of Gr and Pr considered. This procedure was repeated to choose the numerical parameters for other sets of Gr and Pr. These parameters are shown in Table 1.

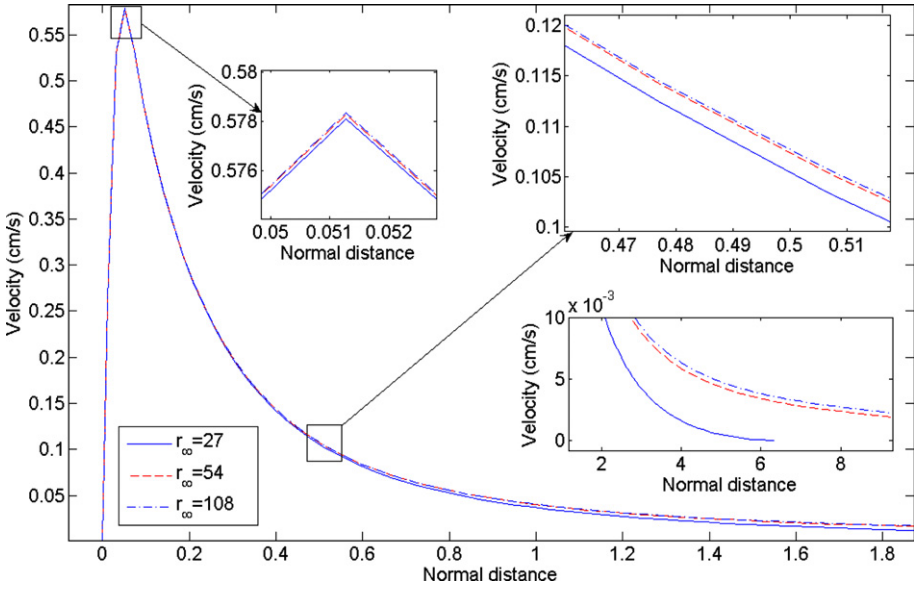

Fig. A3. Radial velocity (cm/s) vs. normal distance for different r_∞ values ($\Delta z = 0.02$, $\Delta\theta = 2°$ and $\Delta t = 0.08$).

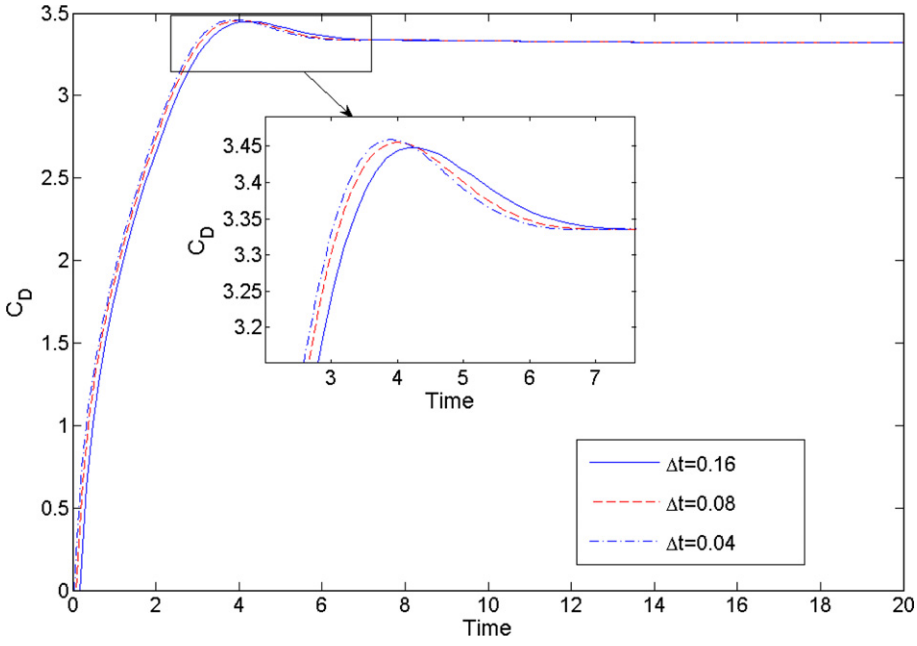

Fig. A4. Variation of C_D with time for different Δt values ($\Delta z = 0.02$, $\Delta\theta = 2°$ and $r_\infty = 54$).

References

Amato, W.S., Tien, C., 1972. Free convection heat transfer from isothermal spheres in water. Int. J. Heat Mass Transfer 15, 327–339.

Chiang, T., Ossin, A., Tien, C.L., 1964. Laminar free convection from a sphere. J. Heat Transfer 86, 537–542.

Churchill, S.W., 1983. Comprehensive theoretical based, correlating equations for free convection from isothermal spheres. Chem. Eng. Commun. 24, 339–352.

Dudek, D.R., Fletcher, T.H., Longwell, J.P., Sarofim, A.F., 1988. Natural convection induced drag forces on spheres at low Grashof numbers: comparison of theory with experiment. Int. J. Heat Mass Transfer 31, 863–873.

Farouk, B., 1983. Natural convection heat transfer from an isothermal sphere. Thermal Sci. 16, 347–364.

Fujii, T., Honda, T., Fujii, M., 1984. A numerical analysis of laminar free convection around an isothermal sphere: finite difference solution of the full Navier–Stokes and energy equations between concentric spheres. Numer. Heat Transfer 7, 103–111.

Gebhart, B., Jaluria, Y., Mahajan, R.L., Sammakia, B., 1988. Buoyancy-Induced Flows and Transport. Hemisphere Publishing Corporation, New York.

Geoola, F., Cornish, A.R.H., 1981. Numerical solution of steady-state free convective heat transfer from a solid sphere. Int. J. Heat Mass Transfer 24, 1369–1379.

Geoola, F., Cornish, A.R.H., 1982. Numerical solution of free convective heat transfer from a sphere. Int. J. Heat Mass Transfer 25, 1677–1687.

Jaluria, Y., Gebhart, B., 1975. On the buoyancy-induced flow arising from a heated hemisphere. Int. J. Heat Mass Transfer 18, 415–431.

Jia, H., Gogos, G., 1996a. Laminar natural convection heat transfer from isothermal sphere. Int. J. Heat Mass Transfer 39, 1603–1615.

Jia, H., Gogos, G., 1996b. Transient Laminar natural convection heat transfer from isothermal sphere. Numer. Heat Transfer A 29, 83–101.

Kranse, A.A., Schenk, J., 1965. Thermal free convection from a solid sphere. Appl. Sci. Res. 15, 397–403.

Kyte, J.R., Madden, A.J., Piret, E.L., 1953. Natural convection heat transfer at reduces pressure. Chem. Eng. Prog. 49, 653–659.

Mathers, W.G., Maddern Jr., A.J., Piret, E.L., 1957. Simultaneous heat and mass transfer in free convection. Ind. Eng. Chem. 49, 961–968.

Patankar, S.V., 1980. Numerical Heat Transfer and Fluid Flow. Hemisphere Publishing Corporation, New York.

Riley, N., 1986. The heat transfer from a sphere in free convective flows. Comput. Fluids 14, 225–237.

Schenk, J., Schenkels, F.A.M., 1968. Thermal free convection from an ice sphere in water. Appl. Sci. Res. 19, 465–476.

Shlien, D.J., Boxman, R.L., 1980. Laminar starting plume temperature field measurement. Int. J. Heat Mass Transfer 24, 919–931.

Singh, S.N., Hasan, M.M., 1983. Free convection about a sphere at small Grashof number. Int. J. Heat Mass Transfer 25, 781–783.

Stewart, W.E., 1971. Asymptotic calculation of free convection in laminar three-dimensional systems. Int. J. Heat Mass Transfer 14, 1013–1031.

Van Doormaal, J., Raithby, G.D., 1984. Enhancements of the simple method for predicting incompressible fluid flows. Numer. Heat Transfer 7, 147–163.

Yuge, T., 1960. Experiments on heat transfer from spheres including combined natural and forced convection. Trans. ASME, 214–220.